Seasonal and interplanetary magnetic field–dependent polar cap contraction during substorm expansion phase

K. M. Laundal,[1] N. Østgaard,[1] H. U. Frey,[2] and J. M. Weygand[3]

Received 5 July 2010; revised 17 August 2010; accepted 24 August 2010; published 30 November 2010.

[1] Recent observations from simultaneous imaging in two hemispheres have shown that the polar caps can attain considerably different shapes as the auroral ovals contract during the substorm expansion phase. We use images from 2770 substorms to study the evolution of the polar cap boundary location statistically. We show that, during the first 26 min after substorm expansion phase onset, the polar cap boundary location depends on seasons, interplanetary magnetic field (IMF) B_y, and IMF B_x. For different signs of B_y, with $|B_y| > 3$ nT, the asymmetry in polar cap boundary observed at onset increases during the expansion phase, consistent with an increase in tail reconnection of field lines with asymmetrical footpoints. When $B_x > 2$ nT and $|B_y| < 2$ nT, the polar cap boundary dawnward of the onset propagates slightly farther poleward compared to negative B_x conditions. In the sunlit hemisphere, the polar cap boundary evolves from a pronounced equatorward displacement at onset to an almost reversed displacement during the expansion phase, compared to substorms observed in darkness. Substorms in the dark hemisphere also have a much more pronounced bulge than substorms in the sunlit hemisphere. If the interpretation of the poleward auroral boundary as being coincident with the open/closed field line boundary (OCB) is correct, the seasonal differences in OCB locations imply seasonal differences in the ionospheric convection during the substorm expansion phase.

Citation: Laundal, K. M., N. Østgaard, H. U. Frey, and J. M. Weygand (2010), Seasonal and interplanetary magnetic field–dependent polar cap contraction during substorm expansion phase, *J. Geophys. Res.*, *115*, A11224, doi:10.1029/2010JA015910.

1. Introduction

[2] It is now well established that the Earth's magnetic field can be perturbed, such as to imply temporal interhemispheric asymmetries in magnetic field line footpoints. This can be clearly seen by observing the aurora simultaneously in the two hemispheres, because similar auroral forms are ionospheric footprints of the same magnetic field lines [e.g., *Østgaard et al.*, 2004]. The distortion of the field lines, which is implied by such observations, is ultimately an effect of the interaction between the Earth's magnetic field and the interplanetary magnetic field (IMF), which is transported away from the sun by the solar wind plasma.

[3] Most of our quantitative knowledge about how the IMF orientation affects interhemispheric asymmetries stems from studies of the onset of auroral substorms [*Liou et al.*, 2001; *Østgaard et al.*, 2005, 2007; *Wang et al.*, 2007]. The onset of a substorm can be seen as a moment of transition between a relatively calm and steady state to a disturbed state. After the onset, the magnetotail becomes more dipolar [e.g., *Baumjohann et al.*, 1999], and excessive reconnection of open magnetic field lines takes place (as observed by, e.g., *Blanchard et al.* [1997]). The significant and global changes that occur in the magnetospheric geometry during this period are also likely to change the prevailing interhemispheric differences.

[4] In two recent studies of conjugate global auroral images during the course of a substorm, large and varying asymmetries in intensity [*Laundal and Østgaard*, 2009] and magnetic field line footpoint [*Laundal et al.*, 2010] were reported. The latter study showed that, as the polar caps contracted during a substorm expansion phase, their shapes became different. The asymmetries were largest in the regions where the polar caps contracted the most. It was shown that the asymmetries could be accounted for, if excitation of ionospheric convection lagged by ≈10 min in one hemisphere compared to the other. The interhemispheric differences in this event could have been due to either the large x component of the IMF (the y component was negligible) or the large seasonal differences.

[5] In the present paper, we investigate statistically the effect of these parameters on auroral poleward propagation. The basis for the study is ~30,000 images from 3943 substorms observed by the Wideband Imaging Camera (WIC) during the lifetime of the Imager for Magnetopause-to-Aurora Global Exploration (IMAGE) satellite and identified by *Frey et al.* [2004] and *Frey and Mende* [2006]. In their study, substorms were defined as clear local auroral bright-

[1]Department of Physics and Technology, University of Bergen, Bergen, Norway.
[2]Space Sciences Laboratory, University of California, Berkeley, California, USA.
[3]Institute of Geophysics and Planetary Physics, University of California, Los Angeles, California, USA.

0148-0227/10/2010JA015910

enings, expanding in latitude and longitude for at least 20 min. In addition, they eliminated events that occurred less than 30 min after the previous onset. This definition is a quantification of the qualitative auroral substorm description presented by *Akasofu* [1964]. Several subsequent substorm studies have substantiated and elaborated on *Akasofu*'s [1964] substorm picture. Of particular importance to the present paper are the studies of the poleward auroral boundary motion during substorms, inferred from global images, both in event studies [*Craven and Frank*, 1987; *Brittnacher et al.*, 1999; *Milan et al.*, 2003] and statistically [*Mende et al.*, 2003; *Gjerloev et al.*, 2008]. One of the findings of *Mende et al.* [2003] and *Gjerloev et al.* [2008] was that the poleward boundary on average propagates the farthest poleward close to the magnetic local time of the substorm onset. It is the aim of the present paper to investigate the dependence of the poleward propagation on seasons and IMF orientation. We focus on the B_x and B_y components of the IMF, because they are believed to affect the two hemispheres differently, producing interhemispheric asymmetries.

[6] We use an automated routine to identify the poleward boundary of the aurora, assumed to be colocated with the open/closed magnetic field line boundary (OCB), at substorm onset and at four time steps up to 26 min into the substorm expansion phase. Looking at average values of the location of this boundary for substorms selected according to the concurrent IMF orientation and seasonal conditions, we find that the morphology of the polar cap during the substorm expansion phase is significantly affected by these parameters. Two mechanisms are proposed to dominate in the production of these asymmetries: tail reconnection of magnetic field lines with footpoints at asymmetrical points in the ionosphere and an asymmetrical response in the ionosphere to excitation of magnetospheric convection.

[7] In section 2, we describe the method that was used to compile the set of OCBs that constitutes the basis for this study, as well as the parameters according to which the substorms are binned. In section 3, average boundaries are presented, and differences due to season and IMF are reported. In section 4, we discuss various mechanisms that might explain these observations, and section 5 concludes the paper.

2. Method

[8] The basis for this study are images from substorm onset and the expansion phase during the 3943 substorms that *Frey et al.* [2004] and *Frey and Mende* [2006] identified in images from the WIC camera on the IMAGE satellite. The IMAGE satellite was launched on 25 March 2000, and it provided data until December 2005. During its first years, the apogee at $\approx 7\ R_E$ was close to the North Pole, and in the later years of the mission, apsidal precession had moved it to the Southern Hemisphere. Most of the substorms in this study are from the first years, because of longer continuous monitoring of the auroral zone, and because of an increasingly inaccurate pointing in the last years of the mission. We made a rough evaluation of the pointing accuracy in each observed substorm, based on the image from substorm onset: First, we removed a few events after manual inspection showing the aurora to be positioned away from the auroral zone. Second, we made sure that the location of the substorm onset, as reported by *Frey et al.* [2004] and *Frey and Mende* [2006], was associated with a local maximum in auroral intensity. Having experimented with different subsets of the resulting data set, we conclude that the inclusion of events late in the IMAGE mission did not change the results significantly, other than contributing to the statistical basis. The images used in this study are from the WIC [*Mende et al.*, 2000]. WIC provided images in the Lyman-Birge-Hopfield wavelength band (140–190 nm). Being mounted on the spinning satellite, it produced images every 123 s (the satellite spin period) and had 10 s integration time.

[9] The Apex coordinate system was used in this study [*Richmond*, 1995]. This coordinate system is based on the International Geomagnetic Reference Field (IGRF), and it produces symmetrical coordinates in the two hemispheres at points that are on the same field lines in the IGRF (the assumed emission height is 130 km). Interhemispheric asymmetries are therefore readily understood as deviations from the IGRF. The difference between Apex and the other commonly used system for auroral zone studies, AACGM, is negligible because these systems are defined almost similarly.

[10] Measurements of the IMF were obtained from the Advanced Composition Explorer spacecraft, which is located in orbit around the L1 point, ~250 R_E sunward of the Earth. The measurements were time shifted to the dayside magnetopause using the method of *Weimer et al.* [2003] and *Weimer* [2004], which uses a minimal variance analysis to include the geometry of the IMF in the time-shift estimate. For each substorm, one value for the components of the IMF was assigned (if data were available): the average in the period 30 min prior to onset, until 20 min after onset. Changing this definition to other time windows close to onset did not produce noticeable differences in our results; neither did imposing constraints on the variability of the IMF.

[11] The substorms were also binned according to seasons, parameterized by the tilt angle of the dipole axis. This is the axis of a best-fit dipole to the IGRF, and it is tilted at an angle of ≈12° with respect to the Earth's rotational axis. The values of the tilt angle therefore range between −35° (minimum at northern winter solstice) and 35° (maximum at northern summer solstice). We use the terms positive tilt, summer, and sunlit interchangeably. However, because the best-fit dipole axis (which also gives the magnetic poles in Apex coordinates) does not pass through the center of the Earth, the tilt angle does not correspond to a unique location of the sunlight terminator seen in Apex coordinates. Having experimented with bins according to UT and various thresholds for the tilt, we can safely say that this discrepancy does not significantly affect our results.

[12] Several studies used auroral images to determine the OCB [e.g., *Milan et al.*, 2007; *Hubert et al.*, 2008; *Boakes et al.*, 2009], and the validity of the method was substantiated by *Carbary et al.* [2003] and *Boakes et al.* [2008] by comparing with boundaries inferred from low-altitude in situ particle precipitation measurements. These authors also found a systematic bias, with the UV-determined boundary being equatorward of the particle boundary at dawn and slightly poleward at dusk. Despite deviations, we use the terms OCB and poleward auroral boundary interchangeably. We do this, believing that, while the actual OCB may be slightly displaced from our observed boundaries, the two boundaries are highly correlated and that any bias is independent of substorm selection criteria (dipole tilt angle and IMF orientation).

[13] To determine the OCB, we use a scheme first suggested by *Carbary et al.* [2003]: The intensity as a function of

latitude is found in 1 h wide magnetic local time (MLT) sectors, with a latitudinal resolution of 1° magnetic latitude. Using a least squares method, the following function is fitted to the resulting intensity profile:

$$f(\lambda) = a_1 e^{-\frac{1}{2}\left(\frac{\lambda - a_2}{a_3}\right)^2} + a_4 + a_5\lambda + a_6\lambda^2, \quad (1)$$

where λ is the magnetic latitude and a_i are constants determined by the least squares method. The Gaussian defined by $a_{1,2,3}$ usually coincides with the aurora, and the quadratic function defined by $a_{4,5,6}$ handles the background, including the sunlight-induced dayglow. In the case of a successful fit, the boundary is assumed to be located one full width at half maximum (FWHM) poleward of the peak of the Gaussian:

$$\lambda_{\mathrm{OCB}} = a_2 + \mathrm{FWHM} = a_2 + 2a_3\sqrt{2\ln(2)}. \quad (2)$$

[14] In applying this method to a large number of intensity profiles (more than 500,000 intensity profiles were fitted for this study), a precise test of the goodness of fit is essential. We use a set of criteria that are slightly different from the criteria used by *Carbary et al.* [2003] and *Boakes et al.* [2008]. Because we rely on these validation studies, we have made a detailed comparison between the two methods of testing the fit. We find that our more liberal criteria yield between two- and fourfold more valid boundaries, without introducing significant errors. An extensive description of our method and a detailed comparison with earlier methods are given in Appendix A.

[15] We note that the use of equation (1) introduces a bias toward single oval events. According to *Gjerloev et al.* [2008], the latitudinal intensity profile during the substorm expansion phase is in general approximated more effectively by a double Gaussian than by a single Gaussian. Double auroral ovals are believed to be most pronounced during the recovery phase of substorms [*Elphinstone et al.*, 1995] and possibly more frequent in substorms that occur during sawtooth events [*Henderson et al.*, 2006]. The results in the present study may therefore be more representative of the expansion phase of isolated substorms. According to *Huang et al.* [2009], isolated substorms are associated with less open flux (OCB at higher latitudes) at substorm onset, and less flux closure during the expansion phase, compared to substorms during sawtooth events.

[16] We are not concerned with the total flux content of the magnetosphere; therefore, we do not need to make an indirect estimate of the boundaries that are not successfully fitted in order to make the OCB a closed loop. Only boundaries satisfying the chosen requirements are used. We only use boundaries from 12 h wide sectors on the nightside and 12 h wide sectors centered at substorm onset. To promote images with good coverage and clear ovals, we discard an image if less than 5 out of these 12 boundaries are successfully identified.

3. Observations

[17] With the aforementioned selection criteria, and with some events late in the IMAGE mission removed because of errors in satellite pointing, we are left with 2770 substorms. Substorms from both hemispheres were used, although the vast majority were observed in the Northern Hemisphere. For the substorms observed in the Southern Hemisphere, we changed the sign of IMF B_y and the tilt angle, assuming that these parameters affect the two hemispheres symmetrically.

3.1. Format of Figures 1, 2, and 3

[18] We present three figures with a common format: one showing the average behavior of all substorms (Figure 1), one where the substorms are binned according to tilt angle (Figure 2), and one where they are binned according to the value of B_y (Figure 3).

[19] For each substorm, we pick nine images: the onset image, and images 3, 4, 6, 7, 9, 10, 12, and 13 after onset. The average OCBs in the onset images are labeled $t = 0$, while boundaries from consecutive images (3 and 4, 6 and 7, etc.) from the expansion phase are labeled by the average time, in minutes, after the onset images: 7.2, 13.3, 19.5, and 25.6 (the satellite spin period is 123 s). Consecutive images are grouped in common bins to increase the statistical significance. Different times are marked by different colors in the plots. The upper limit of 25.6 min was chosen for the present study for the sake of clarity of the figures and because of reduced statistics in the later phase of the substorm. In Figures 2 and 3, where the substorms are chosen according to tilt and B_y, different signs of these parameters are distinguished by dashed and solid lines.

[20] Figures 1a, 2a, and 3a show the average OCBs in 12 one-hour wide magnetic local time sectors, centered at midnight. In Figures 1b–1d, 2b–2d, and 3b–3d, the boundaries contributing to the average were binned by their location relative to the MLT of the substorm onset. Negative numbers indicate boundaries that are duskward of the onset, while positive numbers are dawnward of the onset. In Figures 1c, 1d, 2c, 2d, 3c, and 3d, the substorms were grouped depending on the location of the substorm onset relative to the median of onset locations for the whole data set of *Frey et al.* [2004] and *Frey and Mende* [2006], which is 22.9 MLT. Figures 1c, 2c, and 3c show substorms with onset duskward of the median, whereas Figures 1d, 2d, and 3d show onsets dawnward of the median. The substorm onsets furthest toward noon (at either side of midnight) occurred at 16.9 and 4.2 MLT, constituting the most westward and eastward substorms included in Figures 1c, 2c, and 3c and 1d, 2d, and 3d, respectively.

[21] For the boundaries at onset, and at $\bar{t} = 25.6$, which are the times with the least statistical basis, the thickness of the curves constitute the average plus or minus half the standard error, $s/\sqrt{n}$, where s is the standard deviation in each bin and n is the number of points upon which the average is based. For clarity, we only show the error for the selection criteria giving the least number of valid boundaries (e.g., the sunlit hemisphere, where the Gaussian fit is less likely to succeed). The thickness of these curves can therefore be regarded as the maximum error in each figure (with the single exception of Figure 3c). The bottom of Figures 1–3 shows the number of points used to determineeach of the average boundaries.

3.2. Average OCBs for All Substorms

[22] In Figure 1 we show the average evolution of the OCB for all substorms with acceptable data quality.

[23] On average, substorm onset can be seen as a time when the magnetosphere or ionosphere changes from an undisturbed state to a disturbed state. The black curve in Figure 1a therefore tells us that on average, during quiet conditions, the OCB on the nightside (and likely for the whole oval) is farthest equa-

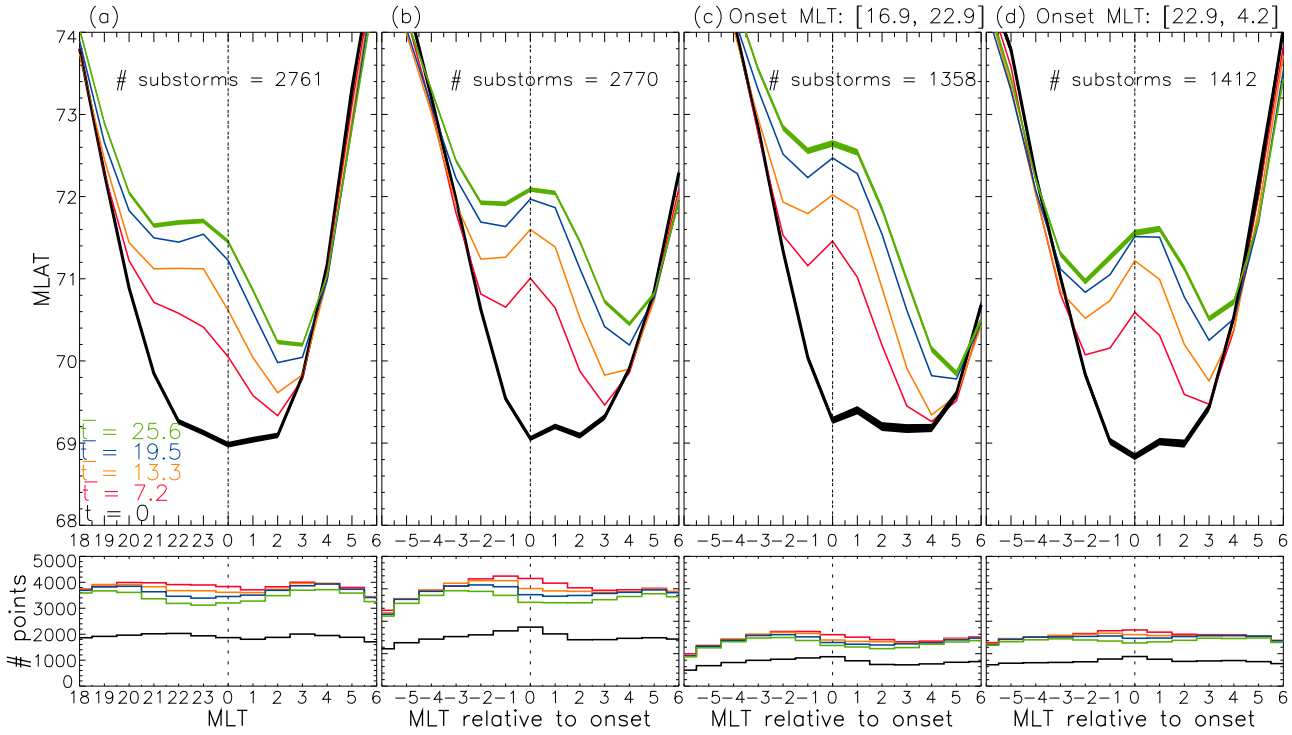

Figure 1. Average open/closed field line boundaries (OCBs) at (a) fixed magnetic local times and (b–d) magnetic local times relative to the MLT of the substorm onset. Different colors indicate the time relative to substorm onset. Figures 1c and 1d are based on substorms with onset westward and eastward of 22.9 MLT, respectively. For the onset curves and the last expansion phase curves, the thickness constitutes the error intervals. The histograms in the bottom row show the number of points upon which each average is based. See section 3.1 for details.

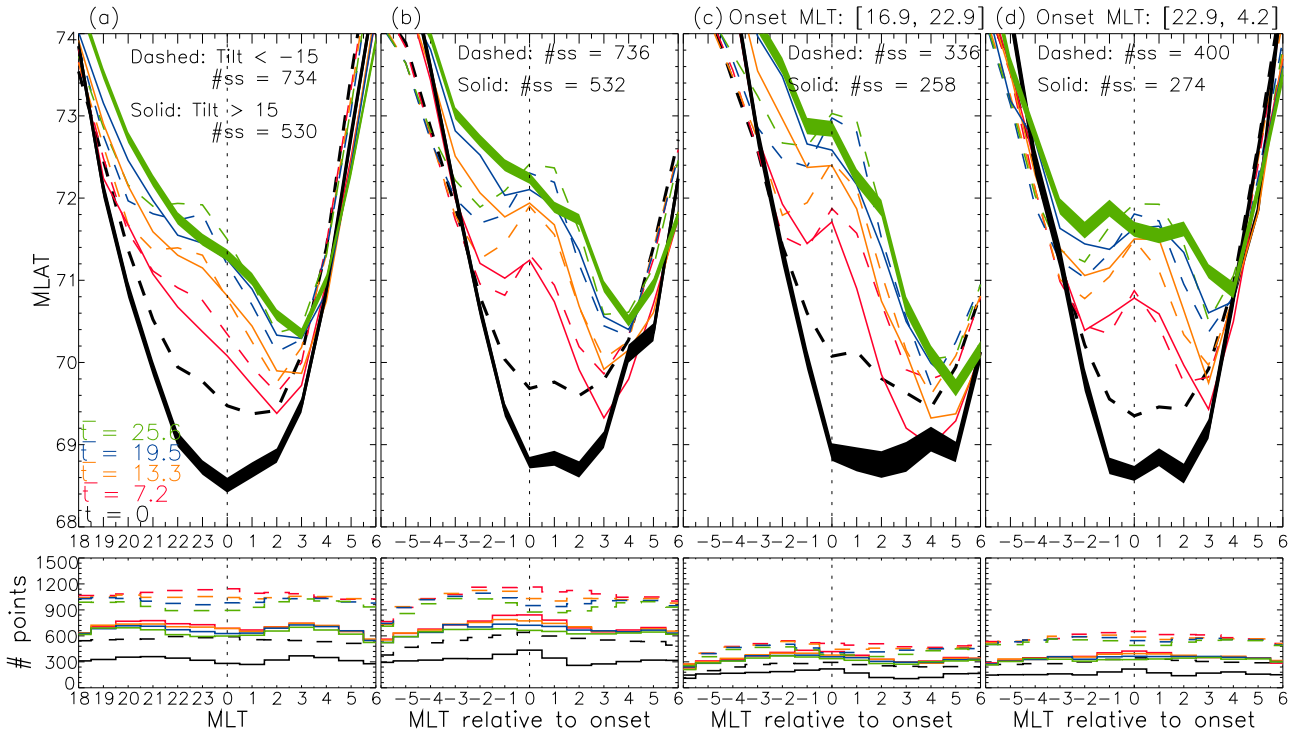

Figure 2. Average OCBs for substorms with onsets during periods when the dipole tilt angle was greater than 15° (solid curves) and less than −15° (dashed curves). The format is the same as in Figure 1. The format is also explained in section 3.1. #ss, number of substorms in each bin.

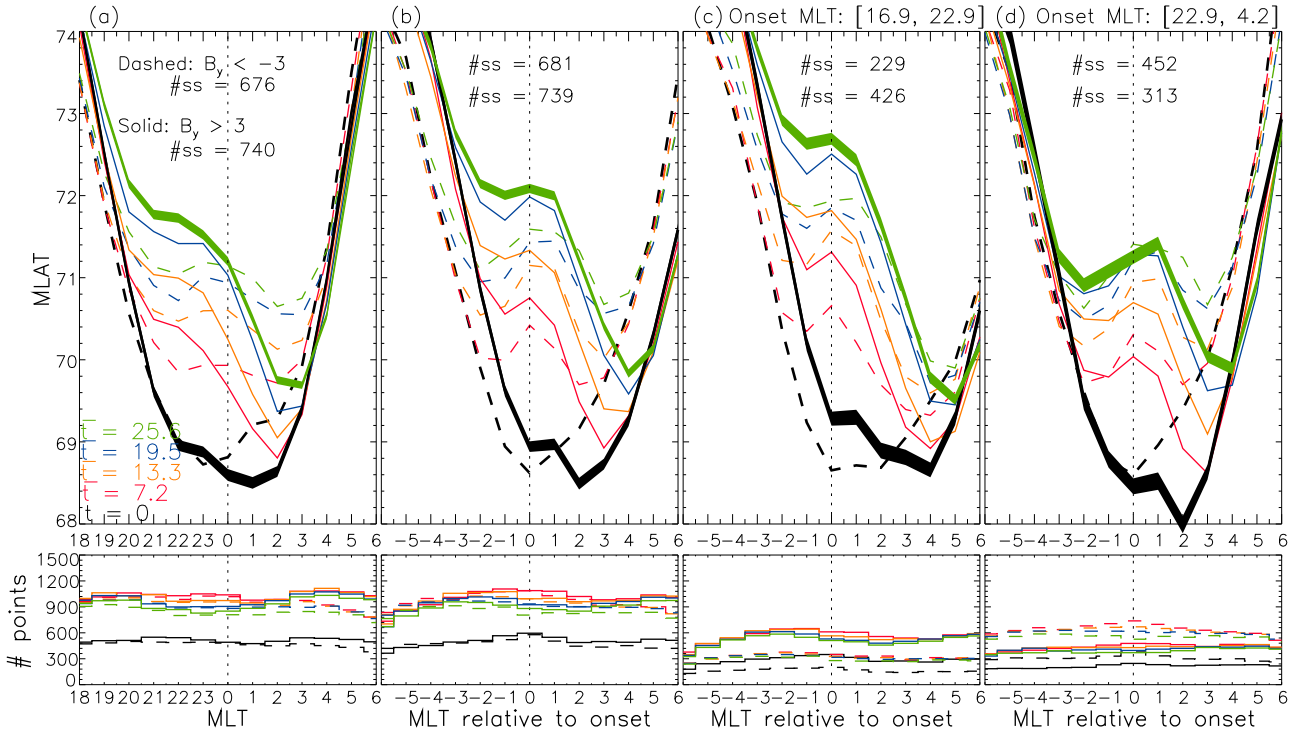

Figure 3. Average OCBs for substorms with onsets when the IMF $B_y < -3$ nT (dashed curves) and IMF $B_y > 3$ nT (solid curves). The format is the same as in Figure 1. The format is also explained in section 3.1.

torward at midnight. This is perhaps not surprising, because we know that the oval generally is displaced toward midnight [*Meng et al.*, 1977], presumably under the influence of the antisunward momentum of the solar wind, and, intuitively, midnight is where this effect converges to a maximum. Another interesting point is that the latitude increases faster with distance from midnight toward dawn than toward dusk. This effect is probably even underestimated in the data, since UV image determination of the OCB has been shown to have a bias toward the equator at the dawnside, compared to the boundaries inferred from low-altitude in situ precipitation measurements [*Carbary et al.*, 2003; *Boakes et al.*, 2008]. We show in section 3.6 that the region dawnward of the onset is associated with a larger increase in the width of the oval than on the dusk side, which could account for some of the observed differences between these regions.

[24] For the $t > 0$ curves, we note the following: (1) The average boundary propagates poleward monotonically for at least 25.6 min after onset. (2) Local maxima are observed in all $t > 0$ curves, but the maximum is much clearer in the plots where we look at the relative MLT (Figures 1a–1c, 2a–2c, and 3a–3c).

[25] These two observations are in very good agreement with what we expect from the works of *Akasofu* [1964], *Mende et al.* [2003], and *Gjerloev et al.* [2008]. The local maximum is the poleward boundary of the auroral bulge, and we refer to this maximum as the bulge from now on. If the interpretation of the poleward boundary as coincident with the OCB is correct, this pattern can only mean that the expansion phase of substorms, on average, is associated with tail reconnection, closing magnetic flux to allow precipitation on closed field lines to expand poleward. Furthermore, the tendency for the poleward propagation to be centered at onset shows that the *X* line on average is located close to the same MLT as the substorm onset.

[26] Figures 1c and 1d show quite different shapes of the OCB, but they both reveal a tendency that the poleward expansion is stronger duskward of the onset. This could be an effect of stronger antisunward convection closer to midnight, transporting the OCB (in the sense described by *Cowley and Lockwood* [1992]) equatorward faster in this region, rectifying the effect of tail reconnection.

[27] No smoothing was applied to the curves in Figure 1 (or in the following figures), but still no clear signs of statistical noise are observed. The $t > 0$ curves all seem to follow the same pattern. This is a good indication that they represent real phenomena and not something which is artificially produced by the fitting and selection methods. Although the curves become less smooth due to the reduced statistics, all the following figures show a consistent pattern, which is hard to discount as artificial.

[28] We can compare the boundary at the substorm onset location to two earlier studies using global UV imagers. *Mende et al.* [2003] looked at the average of 91 substorms seen by IMAGE WIC, and *Gjerloev et al.* [2008] studied 116 substorms seen by the Visible Imaging System (VIS) Earth camera on the Polar satellite. Our statistical data set is more than a factor of 20 larger than in these previous studies. In Table 1, we compare the average poleward boundary at the substorm onset MLT in this study (Figure 1b) and in the studies by *Gjerloev et al.* [2008] and *Mende et al.* [2003]. Compared to the study by *Mende et al.* [2003], we consistently observe higher latitudes, but the difference is only 1° at onset, and decreasing after that. Comparison with the work of

Table 1. Average Magnetic Latitude of the Poleward Boundary of the Aurora at the Onset Magnetic Local Time, as a Function of Time After Substorm Onset

Substorm Time	*Mende et al.* [2003]	*Gjerloev et al.* [2008]	This Study
0	68.0	68.7	69.0
7.2	70.3		71.0
13.3	70.9	71.7[a]	71.6
19.5	71.3		72.0
25.6	71.7	74[a]	72.1

[a]*Gjerloev et al.* [2008] used a normalized substorm time, and the indicated numbers correspond to their $T = 0.5$ and $T = 1.0$, where $T = 1.0$ denotes the end of the expansion phase. Time is given in minutes.

Gjerloev et al. [2008] is more difficult to make, because they applied a normalization technique where $T = 0$ was defined as onset and $T = 1$ as the end of the expansion phase. Their $T = 0$ boundary is only 0.3° equatorward of our onset boundary. In Table 1, we also present the boundary for $T = 0.5$ from the work of *Gjerloev et al.* [2008], which compares well to the $\bar{t} = 13.3$ boundary in our study, and $T = 1.0$, which is farther poleward than our last boundary. It is likely, from the monotonic poleward propagation in Figure 1 and from the work of *Mende et al.* [2003], that the end of the expansion phase on average comes later than 25.6 min after onset, which might explain this discrepancy.

[29] *Mende et al.* [2003] and *Gjerloev et al.* [2008] used a double Gaussian instead of a single Gaussian to fit the auroral oval. As stated earlier, the exclusion of many pronounced double ovals in the present study may represent a bias and contribute to the differences seen in Table 1. *Gjerloev et al.* [2008] also specifically required that the auroral bulge was in darkness. As we show, this selection criterion has a profound influence on the average evolution of the substorm aurora and also contributes to the differences.

3.3. Average OCBs for Substorms Selected According to Dipole Tilt Angle

[30] In Figure 2 we present two separate groups of substorms: Solid lines show substorms occurring when the dipole tilt angle was greater than 15°, and dashed lines show substorms occurring when the dipole tilt angle was less than −15°. For observations in the Southern Hemisphere, we changed the sign of the tilt angle so that positive tilt always corresponds to sunlit conditions. As is clear from the bottom of Figure 2, the Gaussian fit is less likely to succeed in sunlit conditions, and the error intervals (indicated by black and green) are therefore only shown for positive tilt.

[31] We first note that there is a clear tendency that the summer hemisphere OCB is on lower latitudes at substorm onset than in the winter hemisphere. This agrees well with earlier studies [*Oznovich et al.*, 1993], and the presumption that the solar wind momentum, which affects the summer hemisphere more, displaces the oval toward midnight.

[32] Two features stand out in the $t > 0$ curves:

[33] 1. The bulge is much more pronounced in the winter hemisphere. This is seen in all parts of Figures 1–3 and for all $t > 0$. This tendency becomes increasingly clear as t increases. The difference is most pronounced when the OCBs are sorted according to their location relative to the onset MLT.

[34] 2. The asymmetry between seasons seen at onset is severely reduced during the expansion phase, and, at some MLTs, even reversed. We show in section 3.6 that the width of the oval increases faster in the summer, contributing to the apparent decrease in OCB asymmetry. The only MLTs where the winter OCB is leading the summer OCB is at the bulge. The asymmetries in the OCB shown in Figure 2a resemble the seasonal differences in the magnetic latitude of the substorm auroral electrojet, reported by *Wu et al.* [1991]. We discuss possible explanations for the asymmetries in section 4.

[35] Increasing the threshold of 15° gave the expected result of increased differences but gave decreased statistics.

3.4. Average OCBs for Substorms Selected According to the Value of IMF B_y

[36] In Figure 3, we group substorms according to the average value of (time-shifted) IMF B_y in the period 30 min prior to, and 20 min after, onset. Dashed curves had $B_y < -3$ nT, and solid curves had $B_y > 3$ nT. Because of the Parker spiral configuration of the IMF, this figure is very similar to what we get if we select substorms according to $B_x > 3$ nT and $B_x < -3$ nT instead. In section 3.5 we try to isolate the effect of the two components.

[37] At substorm onset, the OCBs are quite similarly shaped for different signs of B_y, but the boundaries for $B_y > 3$ nT are displaced dawnward compared to $B_y < -3$ nT. This is most clear in Figures 3b and 3c. During the expansion phase, the shift remains stable for the boundaries farthest out on the flanks, which are not affected by the emerging bulge. This shift in the boundary location is consistent with a global B_y-dependent displacement of the auroral ovals, in the direction consistent with a net "penetration" of the IMF B_y into the magnetosphere [e.g., *Wing et al.*, 1995] and the "dipole plus uniform field" model described by *Cowley et al.* [1991].

[38] During the expansion phase ($t > 0$), there is a very clear tendency in Figure 3 that the poleward propagation of the OCB is skewed duskward when B_y is positive. A duskward skew was also apparent in Figure 1, where averages of all substorms were considered. However, this tendency seems to increase when B_y is positive. When B_y is negative, a much weaker duskward skew is seen in Figures 3a–3c. In Figure 3d, the $B_y < -3$ nT substorms are even skewed slightly dawnward.

[39] The most striking effect of increasing the $|B_y|$ threshold beyond 3 nT was to move the average boundaries equatorward while decreasing the statistics. Decreasing the threshold led to smaller asymmetries.

3.5. B_x Effect on Substorm Expansion

[40] Figure 4 shows OCBs grouped according to B_y (Figure 4a) and B_x (Figure 4b), with the other component kept less than 2, in absolute value. The format is the same as in Figures 1b, 2b, and 3b. Dashed curves correspond to the Parker spiral sector $B_y < -2$ nT and $B_x > 2$ nT, while solid curves correspond to $B_y > 2$ nT and $B_x < -2$ nT. We notice that Figure 4a is very similar to Figure 3b, as we might expect.

[41] Figure 4b shows that the OCB is consistently on slightly higher latitudes when B_x is positive. This is the exact opposite of what we expect from a "partial penetration" of the IMF into the nightside magnetosphere. Since the boundaries sorted by B_y in the same Parker spiral sector show the opposite asym-

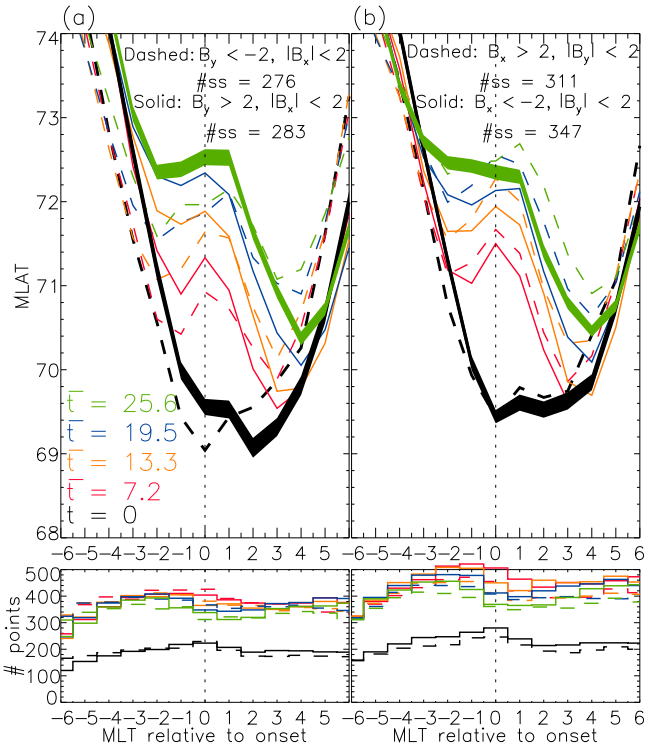

Figure 4. Average OCBs during substorms selected according to the values of (a) B_y and (b) B_x, with the absolute value of the other component kept less than 2. Dashed curves denote substorms when the IMF orientation presumably was in the Parker spiral sector $B_y < 0$, $B_x > 0$, while the solid curves show $B_y > 0$, $B_x < 0$. Figures 4a and 4b show the OCBs at a given distance from the onset MLTs, similar to the format in Figures 1b, 2b, and 3b.

metry, we conclude that this is not an effect of the correlation between B_x and B_y.

[42] The reduced threshold, 2 nT rather than the 3 nT threshold in Figure 3, was chosen to keep the number of substorms in each group high despite the introduction of an additional constraint on the B_y (B_x) component in Figure 4a (Figure 4b).

3.6. Seasonal and IMF Influence on the Full Width at Half Maximum of the Auroral Oval

[43] The definition of the OCB as being one FWHM poleward of the peak of the Gaussian introduces a certain ambiguity: Poleward motion of the OCB could signify a shift in the peak location or a widening of the oval. To distinguish between these effects, we show in Figure 5 the distributions of the FWHM with a similar format and selection criteria as in Figures 1b, 2b, 3b, and 4b. This figure shows that, as expected, the oval becomes increasingly wide at the location of the bulge during the expansion phase. The widening of the oval is more severe dawnward of the onset than duskward of the onset, accounting for at least some of the difference in OCB expansion between these regions.

[44] Figure 5 also shows that the IMF orientation has only a small effect on the FWHM (Figures 5c and 5d). However, during summer, the oval is generally wider than during winter (Figure 5b). Furthermore, the oval widens faster during the expansion phase in the substorms observed in the summer hemisphere. This means that part of the stronger poleward expansion seen in the summer hemisphere, compared to the winter hemisphere, is due to a widening of the oval.

[45] From the validation studies by *Carbary et al.* [2003] and *Boakes et al.* [2008], we cannot be sure that equation (2) is valid for all possible ranges of the FWHM. If this equation for the OCB introduces a FWHM-dependent error, this shortcoming does not affect the qualitative comparison between OCBs for different seasons and IMF orientations unless the FWHM also changes with these parameters. Therefore, the more rapid widening of the auroral oval in the summer hemisphere could indicate that we overestimate the poleward propagation, compared to the winter hemisphere.

[46] This is further supported by considering the reduction of open magnetic flux from substorm onset to $\bar{t}$ = 7.2 indicated by Figure 2b: In the summer hemisphere, the boundary

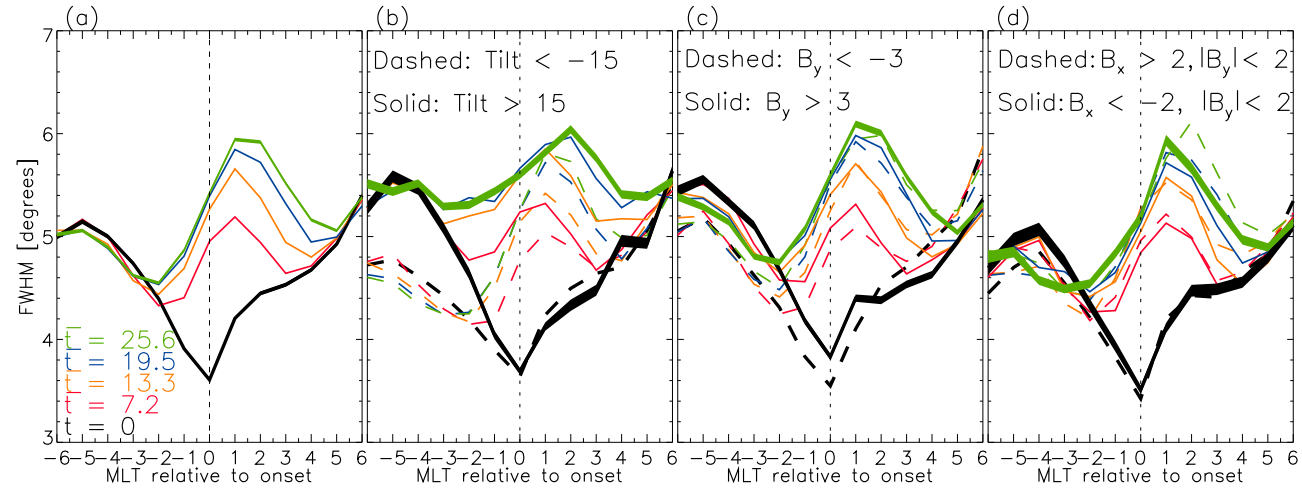

Figure 5. Full width at half maximum (FWHM) of the same intensity profiles used in (a) Figure 1b, (b) Figure 2b, (c) Figure 3b, and (d) Figure 4c. The number of points (n) which each average FWHM is based on is shown below the mentioned figures. The width of the solid $t = 0$ and $\bar{t} = 25.6$ curves shows the standard error of the mean.

propagates further toward the pole, traversing a larger area and hence more magnetic flux, than the OCB in the winter hemisphere. Because the amount of traversed magnetic flux should on average be equal during the two seasons, this difference constitutes a paradox unless it is balanced somewhere else along the OCB, which does not seem to be the case. This paradox could be explained if the widening of the oval causes an overestimation of the poleward propagation in the summer hemisphere compared to that in the winter hemisphere. In that case, the asymmetry in the true OCB location could be less reduced than what is indicated by Figure 2, and the bulge could be even more prominent in the winter hemisphere than in the summer hemisphere.

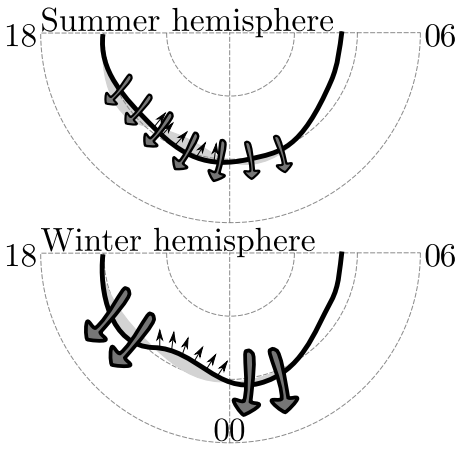

Figure 6. OCBs in the summer and winter hemispheres (black curves) and the interhemispheric differences (shaded regions). The small poleward arrows denote propagation of the bulge caused by tail reconnection. The thick arrows show ionospheric convection, transporting the boundary equatorward. The observed OCB asymmetries seem to imply a more severe suppression of the convection at the bulge in the winter hemisphere compared to the summer hemisphere. In neighboring regions, the convection is stronger in the winter hemisphere.

4. Discussion

[47] For the average OCBs at substorm onset, we have shown the following: (1) The average OCB in the summer hemisphere is displaced equatorward compared to the OCB in the winter hemisphere. (2) When $B_y > 3$ nT, the entire nightside polar cap is displaced toward dawn, compared to $B_y < -3$ nT conditions.

[48] The seasonal asymmetry at onset can be understood as the solar wind momentum affecting the summer hemisphere more than the winter hemisphere. This would expectedly lead to the oval being displaced further toward the nightside in the summer hemisphere, which is what we observe. The displacement between the average boundaries for different signs of B_y are in agreement with the "dipole plus uniform field" model described by *Cowley et al.* [1991].

[49] During the expansion phase of the substorm, the following features are seen in the statistics: (1) The summer hemisphere boundaries propagate poleward faster than the winter hemisphere boundaries, reducing the asymmetry seen at onset. (2) The bulge is much more pronounced in the substorms observed during winter compared to the summer hemisphere substorms. (3) When $B_y > 3$ nT, the poleward propagation is stronger on the duskside of the onset MLT compared to $B_y < -3$ nT conditions. (4) When $B_x > 2$ nT, the OCB is at slightly higher latitudes during the substorm expansion phase compared to that for $B_x < -2$ nT ($|B_y| < 2$ nT), implying a faster poleward propagation following the substorm onset when $B_x > 2$ nT.

[50] These effects are more surprising in terms of the direct effects of the solar wind and IMF on the magnetosphere. However, substorms are associated with significant and rapid changes in the tail, which to some extent can be considered to be internally driven. In the following, we discuss how interhemispheric differences in the shape of the polar cap can arise as a consequence of these changes.

4.1. Asymmetric Ionospheric Response to Magnetospheric Convection

[51] The poleward propagating OCB that is seen in the expansion phase of substorms signifies increased tail reconnection. Tail reconnection allows a reconfiguration of the magnetosphere via convecting flux and plasma [e.g., *Cowley and Lockwood*, 1992]. The enhancement in earthward magnetospheric convection subsequently excites equatorward convection in the ionosphere. However, the time it takes to get the ionosphere in a balanced motion with the magnetosphere likely depends on at least two factors: (1) the ionospheric conductance, which governs the collision frequency, and hence the effective friction with the neutral wind [e.g., *Song et al.*, 2009], as well as the susceptibility of the energy carried by Alfvén waves [*Scholer*, 1970], and (2) the time history of the system, because of the inertia of the prevailing convection. Depending on seasons and IMF, these factors may very well be different in the two hemispheres, causing differences in ionospheric response to the expansion-phase magnetospheric convection. As discussed by *Laundal et al.* [2010], interhemispheric differences in the ionospheric convection lead to interhemispheric differences in magnetic field line footpoints, including field lines on the separatrix.

[52] Ionospheric convection is observable directly from satellites and radars on the ground and indirectly by magnetometers. Quite a few studies of its response to the onset of substorm expansion phases exist. *Lyons et al.* [2001] reported a reduction in convection immediately following the onset. *Bristow and Jensen* [2007] reported an overall reduction but also a rotation to a more meridional flow. *Grocott et al.* [2002] and *Provan et al.* [2004] observed an enhancement of the convection. *Blanchard et al.* [1997] found that there is an increase in ionospheric convection, but it may lag by ~20 min compared to the onset, whereas *Grocott et al.* [2009] found the convection response to depend on the latitude of the substorm onset. It is evident that the ionospheric convection response to substorm onset and expansion can be highly variable. Neither of these studies considered seasonal differences.

[53] Figure 6 shows a conceptual illustration of two main features in the ionospheric convection, which can explain the observed differences in the poleward propagation of the OCB: (1) The equatorward ionospheric convection is generally stronger in the winter hemisphere than in the summer hemisphere, effectively reducing the asymmetry seen at onset. (2) The presence of a bulge in the winter hemisphere, and not in

the summer hemisphere, indicates that the convection is weaker in the bulge region in the winter hemisphere. A local suppression of the ionospheric flow in the substorm bulge was observed by *Provan et al.* [2004], for example. These authors also observed fast flow in the surrounding regions, in agreement with our proposed pattern for the winter hemisphere convection.

[54] If this explanation is true, our observations imply that the flow suppression in the bulge is more prominent in the winter hemisphere. It also implies that, apart from the bulge, the ionospheric convection is stronger in the winter hemisphere. These differences could be caused by the differences in conductance, changing the ionospheric friction and coupling efficiency, as mentioned above. This is in agreement with the work of *Milan et al.* [2009], who pointed out that the brighter the substorm aurora is, the more sluggish the ionospheric convection response will be, because of the increased conductance. During substorms, the conductance is expected to be high and relatively smooth when the ionosphere is sunlit, and low in the dark hemisphere, except for at the bulge, where it is increased by energetic particle precipitation.

[55] In the event study by *Laundal et al.* [2010], in which simultaneous measurements from IMAGE WIC and Polar VIS Earth were used, large asymmetries, which developed during the expansion phase of a substorm, were observed in the polar caps. The asymmetries were largest in the region with the strongest poleward propagation, in good agreement with what we now document statistically. During that event, $|B_y|$ was less than 2 nT, and B_x was strongly positive. The observed asymmetries were in general the opposite of what we would expect from the statistical average OCB for different B_x, shown in Figure 4b. However, there was also a large seasonal difference, with the winter hemisphere boundaries going farther poleward than the summer hemisphere boundaries. This is in agreement with the latitudinal asymmetries in the bulge seen in Figure 2b. This suggests that the asymmetries in the event study were generated by seasonal differences rather than by B_x. We note that the asymmetries that were observed by *Laundal et al.* [2010] were much larger, up to a 5° difference between the two hemispheres, than what is seen in the average case.

4.2. Closing of Field Lines with Asymmetric Footpoints

[56] The orientation of the IMF is also known to cause interhemispheric differences in convection [e.g., *Heppner and Maynard*, 1987; *Ruohoniemi and Greenwald*, 2005; *Haaland et al.*, 2007]. These asymmetries are often attributed to curvature forces acting on newly opened magnetic field lines on the dayside [e.g., *Jørgensen et al.*, 1972; *Cowley et al.*, 1991] and subsequent pressure gradients in the lobes [*Khurana et al.*, 1996]. *Provan et al.* [2004] showed that B_y also affects the convection during substorms. Differences in ionospheric convection due to different signs of B_y, and possibly B_x, may therefore contribute to the observed asymmetries in Figures 3 and 4. However, another effect also exists, which could be important in generating the asymmetries for different signs of B_y. As magnetic field lines approach the tail X line, they are not able to reconnect with field lines with symmetrical footpoints in the opposite hemisphere: For positive (negative) B_y, the northern hemisphere field lines have footpoints duskward (dawnward) of the field lines in the southern hemisphere with which they merge [*Østgaard et al.*, 2004]. We would expect that this leads to an increased poleward propagation on the duskside when $B_y > 0$ and an increased poleward propagation on the dawnside when $B_y < 0$. This is exactly what we observe.

[57] There is no clear analogy to the asymmetric tail reconnection mechanism for different signs of B_x. It does seem reasonable that B_x could have an effect on ionospheric convection; however, this has not yet been firmly established. Figure 4b shows that the OCB close to the MLT of the onset on average ends up at higher latitudes when B_x is positive, indicating that the equatorward convection in this region is stronger when B_x is negative.

4.3. Self-Reinforcing Asymmetries

[58] Another effect, which might explain part of the changing asymmetries seen during the substorm expansion phase, arises from the definition of the Apex coordinate system (and any other similar coordinate systems). In this coordinate system, the amount of magnetic flux in equally wide concentric circles centered at the origin is reduced toward the pole (the amount of flux is constant along these circles, i.e., in the longitudinal direction). Assume that flux closure in the tail is limited to a fixed longitudinal region. If a given amount of magnetic flux closes in the tail, this necessitates a poleward propagation, which encompasses an area corresponding to the magnetic flux which has been closed. The latitudinal dimension of this area (assuming the longitudinal dimension to be fixed), is different, measured in degrees, depending on where the boundary was before the reconnection event. If the boundaries were asymmetrical in the two hemispheres, the asymmetry is expected to be reinforced as flux closes. This may explain some, but likely not all, of the growing asymmetries that we observe for different signs of B_y.

[59] For different signs of tilt angle (Figure 2), the onset asymmetry was observed to be reduced, and even reversed. This can only be explained by different convection in the two hemispheres, and the self-reinforcement effect implies that the convection must be stronger than what is implied by a strictly linear relation between OCB motion in the two hemispheres. For a more detailed explanation of this effect, see the work of *Laundal et al.* [2010].

5. Conclusions

[60] A statistical analysis of auroral images from 2770 substorms has revealed the following:

[61] 1. The OCB propagates poleward monotonically during the first 26 min after substorm onset. The rate of poleward propagation decreased with each 7 min step. At the onset MLT, a local maximum (bulge) in the poleward boundary develops. The poleward propagation is stronger to the west of the onset than to the east.

[62] 2. The poleward expansion of the OCB is faster during summer than during winter, largely reversing the asymmetry seen at onset. The shape of the polar cap is also more circular for summer conditions, with almost no sign of a bulge.

[63] 3. At substorm onset, an almost uniform dawnward shift is seen in the polar cap boundary for $B_y > 3$ nT compared to $B_y < -3$ nT. During the expansion phase, the polar caps have different shapes for the two signs of B_y, attaining a more

pronounced east-west asymmetry with respect to the onset location when $B_y > 3$ nT.

[64] 4. Positive B_x produces a faster poleward propagation, and a more pronounced bulge, than negative B_x. The effect is different from what we would expect if the asymmetry was an effect of the high correlation with B_y.

[65] Rising asymmetries in the OCB for different signs of IMF B_x, B_y, and dipole tilt imply instantaneous differences between the hemispheres, as previously reported by *Laundal et al.* [2010]. The observations presented here further imply that the convection in the first few minutes after substorm onset is different if there are seasonal differences between the hemispheres. Differences in ionospheric convection may also play a role in the observed asymmetries for different signs of B_x and B_y. In the case of B_y, however, much of the growing asymmetry may arise from increased tail reconnection of field lines with asymmetrical footpoints.

[66] A logical next step in exploring the proposed differences in ionospheric convection is to study the seasonal dependence of the convection response to magnetospheric substorms. This may be done in event studies, using conjugate measurements, or statistically. Global MHD models which are able to reproduce the observed asymmetrical polar cap boundary could also be used to test this hypothesis.

Appendix A: Identifying the Open-Closed Boundary

[67] Each image was divided into 1 h wide MLT sectors, producing 24 profiles of intensity as a function of latitude (at 1° resolution). To check that the function $f(\lambda)$, see equation (1), is successfully fitted to an observed intensity profile, we first check that the following criteria are fulfilled:

[68] 1. (c_1) The minimum height of the Gaussian peak, a_1, must be > 50 WIC counts.

[69] 2. (c_2) The position of the peak, $a_1 \in [50°, 85°]$ magnetic latitude.

[70] 3. (c_3) The peak is located at least one full width at half maximum (FWHM) from the last latitude bin in the field of view.

[71] 4. (c_4) The FWHM must be greater than 1.

[72] 5. (c_5) The FWHM must be less than 30% of the latitudes spanned by the field of view.

[73] These requirements primarily ensure that the Gaussian is fitted to a positive, relatively sharp, and fully observed bump in the intensity profile (presumably the oval) and not some artifact of the background. Having passed the above requirements, we make a more subtle test that the fitted profile resembles the observations:

$$\frac{1}{\overline{f_{\text{obs}}}}\sqrt{\sum_{i=1}^{N}\frac{[f(\lambda_i)-f_{\text{obs}}(\lambda_i)]^2}{N}} < 0.2, \tag{A1}$$

that is, the root-mean-square deviation (RMSD), divided by the mean of the observed intensity, must be less than 0.2. The RMSD requirement is a test of how well the function $f(\lambda)$ represents the actual intensity. In the case of double ovals, a single Gaussian is a poor representation, and the profile is in most cases rejected by this requirement. (The conditions c_1 through c_5 would in general not reject a double oval.)

[74] *Carbary et al.* [2003] used the fractional standard deviation (FSD) as a measure of how well the intensity was fitted, instead of the RMSD. The FSD is defined as

$$\sqrt{\frac{1}{N-1}\sum_{i=1}^{N}\left(\frac{f(\lambda_i)-f_{\text{obs}}(\lambda_i)}{f_{\text{obs}}(\lambda_i)}\right)^2}, \tag{A2}$$

which they required should be less than 0.2. The principal difference between these two methods is that the FSD becomes very sensitive to deviations at a few single points if the observed intensity is low (i.e., at the background), whereas the RMSD condition is normalized to the mean. This means that our method is more liberal.

[75] To compare the method of *Carbary et al.* [2003] to the method used in this study, we investigate the effects of the FSD and RMSD acceptance criteria. Equation (2) is intended to give a representation of the poleward boundary of the aurora. Whether this is accomplished can be fairly easily determined by eye. Therefore, we looked at 4000 intensity profiles: 2000 randomly picked from the entire data set and 2000 that include the substorm onset aurora. Each profile was categorized as a successful or a failed boundary determination, constituting a set answer to which the automatic methods can be compared. In the case of random profiles (substorm onset profiles), 533 (133) out of 2000 fitted profiles gave a poor representation of the boundary.

[76] The effects of the acceptance criteria are summarized in Table A1. The criteria are given in the first row and columns: (1) $\bigcap_{i=1}^{5} c_i$, requirements c_1 to c_5 are all fulfilled; (2) the fractional standard deviation is less than 0.2; and (3) the RMSD divided by the mean of the observed intensity (RMSD′) is less than 0.2. The top half of the table is based on the random profiles, whereas the bottom half is based on the substorm onset profiles. The top numbers in each cell show the percentage that was accepted by the given combination of criteria. That is, the FSD requirement accepted 32.7% (22.5%) of the functions fitted to random (onset) intensity profiles, whereas the RMSD requirement accepted 77.8% (88.0%) of the fits (diagonal cells). The condition used in this study is that both the RMSD and conditions c_1 through c_5 are fulfilled. This combination accepted 63.2% (86.9%) of the fitted functions in the case of random (onset) profiles (Table A1, top right). Compared to the method of *Carbary et al.* [2003], we get approximately twofold (random) and fourfold (onset) more accepted boundaries.

[77] An important question with respect to the statistical analysis is whether our method includes a large amount of erroneously accepted boundaries. The numbers in parentheses show the percentage of the boundaries that were accepted by the given combination of criteria, which should have been rejected. Out of the boundaries accepted by both the RMSD criterion and the c_i criteria, 4.3% (3.5%) should have been rejected for random (onset) profiles. Only 1.6% (0.6%) of the boundaries accepted by *Carbary et al.*'s [2003] conditions should have been rejected. Although our method accepts a larger fraction of wrong boundaries, the contribution to the average (which we are interested in) is small: If there are, say, 5% wrong boundaries, which represents a systematic error of 5° (we saw no tendency toward a systematic error while manually inspecting the boundaries, and many of the poor

Table A1. Success Rate and Fraction of Erroneously Accepted Boundaries for Various Combinations of Goodness-of-Fit Tests[a]

	RMSD′ < 0.2	FSD < 0.2	$\bigcap_{i=1}^{5} c_i$
Random Profiles			
RMSD′ < 0.2	77.8	32.5	63.2
	(18.9)	(7.9)	(4.3)
FSD < 0.2		32.7	26.7
		(7.2)	(1.6)
$\bigcap_{i=1}^{5} c_i$			78.7
			(7.4)
Substorm Onset Profiles			
RMSD′ < 0.2	88.0	22.5	86.9
	(4.3)	(0.9)	(3.5)
FSD < 0.2		22.5	22.0
		(0.9)	(0.6)
$\bigcap_{i=1}^{5} c_i$			97.5
			(4.5)

[a]The top half of the table is based on manual inspection of 2000 boundaries randomly chosen from the full data set used in this paper. The bottom half of the table is based on 2000 profiles, which include the substorm onset. $\bigcap_{i=1}^{5} c_i$ denotes the requirement that conditions c_1 through c_5 (see text) are all fulfilled. The top right corners of the two halves correspond to the requirements that were used in this study. RMSD′, root-mean-square deviation, divided by the mean of the observed intensity; FSD, fractional standard deviation. Success rates are the numbers not in parenthesis. The fraction of erroneously accepted boundaries numbers are in parenthesis.

fits produced errors smaller than 5°), the overall contribution to the average is $0.05 \times 5° = 0.25°$. This is less than the error with which UV images can determine the OCB, according to *Carbary et al.* [2003] and *Boakes et al.* [2008]. Thus, we conclude that our method introduces negligible new errors when compared with previous methods, while significantly increasing the number of boundaries that can be used in the statistical analysis. As a final test of the validity of our method, we did a comparison of the figures presented in the present paper, with similar figures with the RMSD criterion replaced by the FSD criterion (not shown). The same patterns clearly emerged, although they appeared less smooth, which is expected from the reduced statistics.

[78] We note that our method differs from that of *Carbary et al.* [2003] also by the absolute intensity requirement (c_1), which in our case is so low that it has practically no other effect than making sure the Gaussian peak is positive. We also neglected the requirement that the Gaussian should be no smaller than 20% of the background at the peak location: $a_1/(a_4 + a_5a_2 + a_6a_2^2) > 0.2$. This requirement leads to the rejection of many well-defined boundaries. For instance, if a peak of 400 WIC counts is embedded in a sunlit background of 2000 counts, it would be automatically rejected by this requirement, although such a scenario often involves smooth profiles that are easily fitted by $f(\lambda)$. For this reason, and because sunlight or darkness is an important selection criterion in our analysis, we omit this requirement.

[79] **Acknowledgments.** The authors thank S. B. Mende and the IMAGE FUV team for the use of IMAGE FUV data. We thank C. Smith for the ACE magnetic field data and D. McComas for the ACE solar wind data. We also thank Arne Åsnes for contributing to the processing of the ACE data. This study was financed by the IPY-ICESTAR project, The Research Council of Norway, contract 176045/S30.

[80] Robert Lysak thanks Daniel Weimer and another reviewer for their assistance in evaluating this paper.

References

Akasofu, S.-I. (1964), The development of the auroral substorm, *Planet. Space Sci.*, *12*, 273–282.

Baumjohann, W., M. Hesse, S. Kokobun, T. Mukai, T. Nagai, and A. A. Petrukovich (1999), Substorm dipolarization and recovery, *J. Geophys. Res.*, *104*, 24,995–25,000.

Blanchard, G. T., L. R. Lyons, and O. de la Beaujardiére (1997), Magnetotail reconnection rate during magnetospheric substorms, *J. Geophys. Res.*, *102*, 24,303–24,312.

Boakes, P. D., S. E. Milan, G. A. Abel, M. P. Freeman, G. Chisham, B. Hubert, and T. Sotirelis (2008), On the use of IMAGE FUV for estimating the latitude of the open/closed magnetic field line boundary in the ionosphere, *Ann. Geophys.*, *26*, 2759–2769.

Boakes, P. D., S. E. Milan, G. A. Abel, M. P. Freeman, G. Chisham, and B. Hubert (2009), A statistical study of the open magnetic flux content of the magnetosphere at the time of substorm onset, *Geophys. Res. Lett.*, *36*, L04105, doi:10.1029/2008GL037059.

Bristow, W. A., and P. Jensen (2007), A superposed epoch study of SuperDARN convection observations during substorms, *J. Geophys. Res.*, *112*, A06232, doi:10.1029/2006JA012049.

Brittnacher, M., M. Fillingim, G. Parks, G. Germany, and J. Spann (1999), Polar cap area and boundary motion during substorms, *J. Geophys. Res.*, *104*, 12,251–12,262.

Carbary, J. F., T. Sotirelis, P. T. Newell, and C.-I. Meng (2003), Auroral boundary correlations between UVI and DMSP, *J. Geophys. Res.*, *108*(A1), 1018, doi:10.1029/2002JA009378.

Cowley, S. W. H., and M. Lockwood (1992), Excitation and decay of solar wind-driven flows in the magnetosphere-ionosphere system, *Ann. Geophys.*, *10*, 103–115.

Cowley, S. W. H., J. P. Morelli, and M. Lockwood (1991), Dependence of convective flows and particle precipitation in the high-latitude dayside ionosphere on the *x* and *y* components of the interplanetary magnetic field, *J. Geophys. Res.*, *96*, 5557–5564.

Craven, J. D., and L. A. Frank (1987), Latitudinal motions of the aurora during substorms, *J. Geophys. Res.*, *92*, 4565–4573.

Elphinstone, R. D., et al. (1995), The double oval UV auroral distribution. 1. Implications for the mapping of auroral arcs, *J. Geophys. Res.*, *100*, 12,075–12,092.

Frey, H. U., and S. B. Mende (2006), Substorm onsets as observed by IMAGE-FUV, in *Substorms VIII: Proceedings of the 8th International Conference on Substorms*, pp. 71–76, Univ. of Calgary Press, Calgary, Alberta, Canada.

Frey, H. U., S. B. Mende, V. Angelopoulos, and E. F. Donovon (2004), Substorm onset observations by IMAGE-FUV, *J. Geophys. Res.*, *109*, A10304, doi:10.1029/2004JA010607.

Gjerloev, J. W., R. A. Hoffman, J. B. Sigwarth, L. A. Frank, and J. B. H. Baker (2008), Typical auroral substorm: A bifurcated oval, *J. Geophys. Res.*, *113*, A03211, doi:10.1029/2007JA012431.

Grocott, A., S. W. H. Cowley, J. B. Sigwarth, J. F. Watermann, and T. K. Yeoman (2002), Excitation of twin-vortex flow in the nightside high-latitude ionosphere during an isolated substorm, *Ann. Geophys.*, *20*, 1577–1601.

Grocott, A., J. A. Wild, S. E. Milan, and T. K. Yeoman (2009), Superposed epoch analysis of the ionospheric convection evolution during substorms: Onset latitude dependence, *Ann. Geophys.*, *27*, 591–600.

Haaland, S. E., G. Paschmann, M. Forster, J. M. Quinn, R. B. Torbert, C. E. McIlwain, H. Vaith, P. A. Puhl-Quinn, and C. A. Kletzing (2007), High-latitude plasma convection from cluster EDI measurements: Method and IMF-dependence, *Ann. Geophys.*, *25*, 239–253.

Henderson, M. G., et al. (2006), Substorms during the 10–11 August 2000 sawtooth event, *J. Geophys. Res.*, *111*, A06206, doi:10.1029/2005JA011366.

Heppner, J. P., and N. C. Maynard (1987), Empirical high-latitude electric field models, *J. Geophys. Res.*, *92*, 4467–4489.

Huang, C.-S., A. D. DeJong, and X. Cai (2009), Magnetic flux in the magnetotail and polar cap during sawteeth, isolated substorms, and steady magnetospheric convection events, *J. Geophys. Res.*, *114*, A07202, doi:10.1029/2009JA014232.

Hubert, B., S. E. Milan, A. Grocott, S. W. H. Cowley, and J. C. Gerard (2008), Open magnetic flux and magnetic flux closure during sawtooth events, *Geophys. Res. Lett.*, *35*, L23301, doi:10.1029/2008GL036374.

Jørgensen, T. S., E. Friis-Christensen, and J. Wilhjelm (1972), Interplanetary magnetic-field directions and high-latitude ionospheric currents, *J. Geophys. Res.*, *77*, 1976–1977.

Khurana, K. K., R. J. Walker, and T. Ogino (1996), Magnetospheric convection in the presence of interplanetary magnetic field B_y: A conceptual model and simulations, *J. Geophys. Res.*, *101*, 4907–4916.

Laundal, K. M., and N. Østgaard (2009), Asymmetric auroral intensities in the Earth's Northern and Southern hemispheres, *Nature*, *460*, 491–493, doi:10.1038/nature08154.

Laundal, K. M., N. Østgaard, K. Snekvik, and H. U. Frey (2010), Interhemispheric observations of emerging polar cap asymmetries, *J. Geophys. Res.*, *115*, A07230, doi:10.1029/2009JA015160.

Liou, K., P. T. Newell, and C.-I. Meng (2001), Seasonal effects on auroral particle acceleration and precipitation, *J. Geophys. Res.*, *106*, 5531–5542.

Lyons, L. R., J. M. Ruohoniemi, and G. Lu (2001), Substorm-associated changes in large-scale convection during the November 24, 1996, Geospace Environment Modeling event, *J. Geophys. Res.*, *106*, 397–405.

Mende, S. B., et al. (2000), Far ultraviolet imaging from the IMAGE spacecraft: 2. Wideband FUV imaging, *Space Sci. Rev.*, *91*, 271–285.

Mende, S. B., H. U. Frey, B. J. Morsony, and T. J. Immel (2003), Statistical behavior of proton and electron auroras during substorms, *J. Geophys. Res.*, *108*(A9), 1339, doi:10.1029/2002JA009751.

Meng, C.-I., R. H. Holzworth, and S.-I. Akasofu (1977), Auroral circle: Delineating the poleward boundary of the quiet auroral belt, *J. Geophys. Res.*, *82*, 164–172.

Milan, S. E., M. Lester, S. W. H. Cowley, K. Oksavik, M. Brittnacher, R. A. Greenwald, G. Sofko, and J.-P. Villain (2003), Variations in the polar cap area during two substorm cycles, *Ann. Geophys.*, *21*, 1121–1140.

Milan, S. E., G. Provan, and B. Hubert (2007), Magnetic flux transport in the Dungey cycle: A survey of dayside and nightside reconnection rates, *J. Geophys. Res.*, *112*, A01209, doi:10.1029/2006JA011642.

Milan, S. E., A. Grocott, C. Forsyth, S. M. Imber, P. D. Boakes, and B. Hubert (2009), A superposed epoch analysis of auroral evolution during substorm growth, onset and recovery: Open magnetic flux control of substorm intensity, *Ann. Geophys.*, *27*, 659–668.

Østgaard, N., S. B. Mende, H. U. Frey, T. J. Immel, L. A. Frank, J. B. Sigwarth, and T. J. Stubbs (2004), Interplanetary magnetic field control of the location substorm onset and auroral features in the conjugate hemisphere, *J. Geophys. Res.*, *109*, A07204, doi:10.1029/2003JA010370.

Østgaard, N., N. A. Tsyganenko, S. B. Mende, H. U. Frey, T. J. Immel, M. Fillingim, L. A. Frank, and J. B. Sigwarth (2005), Observations and model predictions of substorm auroral asymmetries in the conjugate hemispheres, *Geophys. Res. Lett.*, *32*, L05111, doi:10.1029/2004GL022166.

Østgaard, N., S. B. Mende, H. U. Frey, J. B. Sigwarth, A. Aasnes, and J. Weygand (2007), Auroral conjugacy studies based on global imaging, *J. Atmos. Sol. Terr. Phys.*, *69*, 249–255.

Oznovich, I., R. W. Eastes, R. E. Hoffman, M. Tur, and I. Glaser (1993), The aurora at quiet magnetospheric conditions: Repeatability and dipole tilt angle dependence, *J. Geophys. Res.*, *98*, 3789–3797.

Provan, G., M. Lester, S. B. Mende, and S. E. Milan (2004), Statistical study of high-latitude plasma flow during magnetospheric substorms, *Ann. Geophys.*, *22*, 3607–3624.

Richmond, A. D. (1995), Ionospheric electrodynamics using magnetic apex coordinates, *J. Geomagn. Geoelectr.*, *47*, 191–212.

Ruohoniemi, J. M., and R. A. Greenwald (2005), Dependencies of high-latitude plasma convection: Consideration of interplanetary magnetic field, seasonal, and universal time factors in statistical patterns, *J. Geophys. Res.*, *110*, A09204, doi:10.1029/2004JA010815.

Scholer, M. (1970), On motion of artificial ion clouds in magnetosphere, *Planet. Space Sci.*, *18*, 977.

Song, P., V. M. Vasyliunas, and X.-Z. Zhou (2009), Magnetosphere-ionosphere/thermosphere coupling: Self-consistent solutions for a one-dimensional stratified ionosphere in three-fluid theory, *J. Geophys. Res.*, *114*, A08213, doi:10.1029/2008JA013629.

Wang, H., H. Lühr, S. Y. Ma, and H. U. Frey (2007), Interhemispheric comparison of average substorm onset locations: Evidence for deviation from conjugacy, *Ann. Geophys.*, *25*, 989–999.

Weimer, D. R. (2004), Correction to "Predicting interplanetary magnetic field (IMF) propagation delay times using the minimum variance technique," *J. Geophys. Res.*, *109*, A12104, doi:10.1029/2004JA010691.

Weimer, D. R., D. M. Ober, N. C. Maynard, M. R. Collier, D. J. McComas, N. F. Ness, C. W. Smith, and J. Watermann (2003), Predicting interplanetary magnetic field (IMF) propagation delay times using the minimum variance technique, *J. Geophys. Res.*, *108*(A1), 1026, doi:10.1029/2002JA009405.

Wing, S., P. T. Newell, D. G. Sibeck, and K. B. Baker (1995), A large statistical study of the entry of interplanetary magnetic field *y*-component into the magnetosphere, *Geophys. Res. Lett.*, *22*, 2083–2086.

Wu, Q., T. J. Rosenberg, L. J. Lanzerotti, C. G. Maclennan, and A. Wolfe (1991), Seasonal and diurnal variations of the latitude of the westward auroral electrojet in the nightside polar cap, *J. Geophys. Res.*, *96*, 1409–1419.

H. U. Frey, Space Sciences Laboratory, University of California, 7 Gauss Way, Berkeley, CA 94720–7450, USA. (hfrey@ssl.berkeley.edu)

K. M. Laundal and N. Østgaard, Department of Physics and Technology, University of Bergen, Allegaten 55, N-5007 Bergen, Norway. (karl.laundal@ift.uib.no; nikolai.ostgaard@ift.uib.no)

J. M. Weygand, Institute of Geophysics and Planetary Physics, University of California, Los Angeles, CA, USA. (jweygand@igpp.ucla.edu)